Experimental and Numerical Approaches to Controlling CO_2 Laser Micro-Ablation of Fused Silica Glass: Surface Profile and Heat-Affected Zone

L. A. Vazquez-Zuniga[1], S. Monneret[1], J.F. Gleyze[2], P. Cormont[2], and L. Gallais[*1]

[1]*Aix Marseille Univ, CNRS, Centrale Med, Institut Fresnel, Marseille, France*
[2]*CEA-CESTA, 15 Avenue des Sablières, CS 60001, F33116 Le Barp Cedex, France*
[*]*Corresponding author's e-mail: laurent.gallais@fresnel.fr*

Fused silica is a cornerstone material in photonics thanks to its outstanding optical, thermal and mechanical robustness. Its surface can be selectively functionalized with CO_2 lasers, whose strong infrared absorption confines energy to a thin layer and enables precise thermal effects—from annealing to ablation and laser polishing. Here we quantify how CO_2 laser parameters govern crater morphology and the surrounding heat-affected zone (HAZ). Pits were machined with a 180 µm-diameter focused beam using single pulses from 10 µs to 2 s across the evaporative regime. Optical profilometry coupled with quantitative phase microscopy maps both topography and subsurface refractive-index changes, providing a rapid, non-destructive assessment of the HAZ. We show that, for a fixed removal depth, crater aspect ratio and HAZ width can be tuned independently by modulating pulse width and power: short, high-fluence pulses minimize collateral damage and favor smooth profiles. A two-dimensional finite-element model reproduces the transient temperature field and corroborates the experimental trends. The resulting guidelines enable high-precision CO_2 laser processing of fused silica while mitigating HAZ and associated thermo-mechanical stress, microcracking and debris—crucial for generation of advanced optical components.

DOI: 10.2961/ilmn.2026.01.2005
Keywords: CO_2 laser processing, fused silica, laser damage

1. Introduction

Fused silica is a key material in photonics and optics, particularly in high-power laser systems, owing to its combination of exceptional optical and physical properties. Its ultra-high purity minimizes scattering and absorption losses, and its extremely low coefficient of thermal expansion ensures dimensional stability under varying thermal loads. In addition, fused silica can be polished to extremely high surface quality, making it suitable for demanding optical applications. Its high laser damage threshold—across both pulsed UV and continuous-wave (CW) infrared regimes—makes it particularly well-suited for applications involving high intensity lasers [1,2].

The surface of fused silica optics is typically prepared using mechanical shaping and polishing, often followed by chemical or plasma etching to achieve the desired surface structure [3-5]. However, these processes can inadvertently introduce defects, such as micro-scratches, sub-surface fractures, or polishing residues [6]. These imperfections are known to act as precursors for laser-induced damage, particularly under repeated exposure to high UV fluence. Over time, these sites can grow, reducing optical performance or rendering components unusable [7,8].

To address this, localized surface treatments have been developed to "heal" or mitigate these damage sites. Among these, laser-based techniques have gained attention due to their non-contact nature and ability to perform precise, localized processing [9]. By selectively melting or ablating small surface regions, laser treatment can remove or stabilize defects, restoring the surface properties to a state comparable to pristine silica [10-13].

CO_2 laser processing is especially attractive for such treatments. Fused silica exhibits strong absorption in the infrared, allowing efficient energy deposition in a thin surface layer. This localized heating can induce a variety of thermal effects—melting, reflow, densification, or evaporation—making it suitable for polishing, micromachining, or defect mitigation [14-20]. Furthermore, with appropriate control over laser parameters such as pulse duration, energy, and repetition rate, thermal effects can be finely tuned to achieve sub-micron precision with minimal collateral damage.

However, laser-induced surface modification also presents challenges. Uncontrolled heating can lead to residual stress, redeposition of debris, refractive index changes due to densification, or the formation of rims on the heated sites. Minimizing such side effects requires a detailed understanding of the thermal response of fused silica under different irradiation conditions.

In this context, our work aims to deepen the understanding of how CO_2 laser parameters influence surface morphology and the extent of the heat-affected zone (HAZ) in fused silica. Unlike typical laser processing setups that use beam scanning and multiple passes, we focus on single-pulse, isolated laser sites to simplify both the experimental and modeling approaches. Using a focused CO_2 laser beam (180 µm diameter) and pulse durations ranging from 10 µs to several

seconds, we systematically investigate surface modifications under densification and evaporative regimes. The resulting craters are analyzed in terms of shape, depth, and HAZ characteristics.

To characterize the modifications, we employ a combination of optical profilometry and quantitative phase microscopy, enabling both surface topography and subsurface optical property changes to be assessed. This dual approach allows for a comprehensive evaluation of the thermally induced refractive index changes within the heat affected zone. Furthermore, a two-dimensional finite element thermal model is applied to simulate the transient temperature field and associated changes in properties to support interpretation of the experimental data. The insights gained from this study contribute to optimizing CO_2 laser processing for high-precision surface treatment of fused silica optics, with particular relevance for components operating under high UV laser fluence where defect control is critical.

2. Materials and Methods

This section outlines the experimental methodology, including the selection and preparation of high-purity silica samples, the laser processing system configuration, and the metrology tools used to characterize the laser-induced modifications.

2.1 Samples

The material used in this study is high-purity synthetic amorphous silicon dioxide (7980 Standard Grade, Corning), classified as Type III silica according to standard industry nomenclature (fused silica). It is produced by flame hydrolysis and characterized by a hydroxyl (OH) content between 800 and 1000 ppm. This compositional detail is significant, as the OH content influences several key physical properties of silica, including viscosity, characteristic temperatures such as the annealing and softening points, and density [21,22]. Consequently, different types of fused silica may exhibit varying responses to laser processing [23].

The samples were circular disks, 50.8 mm in diameter and 5 mm thick, optically polished to a 20-10 Scratch-Dig specification and a surface flatness of λ/10.

2.2 Laser processing

A schematic of the laser processing setup is shown in Figure 1. The system is an evolution of the one detailed in [24].

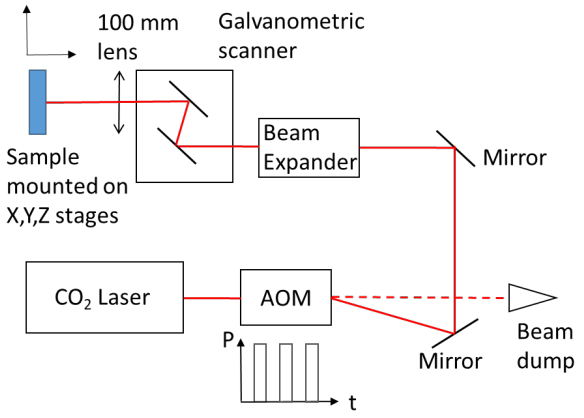

Fig. 1 Schematic of the CO_2 laser processing system.

The laser source is a RF-excited CO_2 laser (Luxinar SR10i, UK) emitting at 10.6 μm, with slight spectral variations in the range 10.17–10.7 μm as per manufacturer specifications. It delivers a quasi-continuous wave output power of 120 W (RF-excitation is modulated at 130 kHz with a duty cycle of 60% resulting in a quasi-cw laser power with a small modulation index). Active power feedback ensures output stability within 2% peak-to-peak and 0.5% RMS.

Pulse generation is achieved using the first diffraction order of an acousto-optic modulator (AOM, 1209-9-1010M, Isomet Corp., USA), which allows control of pulse width ($\Delta\tau$). The beam path includes gold-coated mirrors (NB2L01, Thorlabs, USA) for transport and alignment, followed by a beam expander (BET0103A, Wavelength Opto-Electronics, China) to match the laser beam size with the 14 mm entrance aperture of the galvanometer scanner (ProSeries II, Cambridge Technology, USA), which is equipped with a 100 mm focal length ZnSe focusing lens.

At focus, the CO_2 laser beam exhibits a Gaussian spatial profile with a diameter of 180 μm ($1/e^2$), measured using a scanning slit profiler (NanoScan NS2S-PY/9/5, Ophir Optronics Solutions). The beam ellipticity exceeds 0.85. The sample is mounted on precision translation stages (8MT, Standa, Lithuania), allowing accurate alignment and focus adjustment relative to the laser beam.

2.3 Optical profilometry

Surface topography of the laser-processed regions was measured using a coherence correlation interferometric optical profilometer (NewView 7300, Zygo). The system was configured with a 10X / 0.3 NA objective, yielding a lateral measurement area of 700 μm × 530 μm and a lateral resolution of 0.95 μm. The vertical resolution is sub-nanometric (0.1 nm), enabling precise quantification of shallow surface features and crater profiles.

2.4 Phase microscopy

CO_2 laser irradiation induces structural changes in fused silica, forming a heat-affected zone (HAZ) with altered physical properties. These changes include localized densification, which leads to a variation in refractive index [25,26]. Several techniques can be employed to characterize this refractive index change, such as Raman spectroscopy [27,28], prism coupling [29], or etching-based methods which exploit the correlation between etch rate and fictive temperature [30].

In this study, we employed quantitative phase microscopy (QPM) to characterize the optical phase shift introduced by the modified material, which correlates with refractive index and thickness variations. The QPM setup is detailed in Figure 2. This technique enables non-destructive, high-resolution mapping of the phase retardation induced by the laser treatment, providing valuable insight into the depth and magnitude of structural changes within the HAZ.

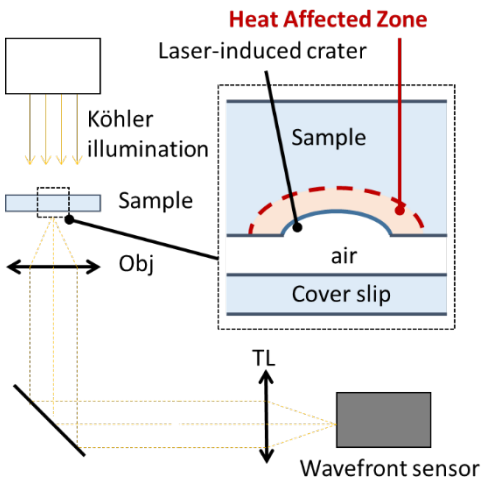

Fig. 2 Schematic of the quantitative phase microscope.

The experimental setup used for quantitative phase microscopy is based on the configuration detailed in [31]. It consists of an inverted microscope (TE2000-U, Nikon, Japan), equipped with a 20× objective with a numerical aperture of 0.5, and a Köhler white-light illumination system to ensure uniform and high-contrast imaging. A commercial wavefront sensor (SID4Bio, Phasics, France), based on quadriwave lateral shearing interferometry, was mounted on the video port of the microscope. Combination of wavefront measurement and imaging enables the display of a so-called optical path difference (OPD) distribution across the field of view with high sensitivity and spatial resolution [32].

To isolate the optical effects induced by laser processing, a differential measurement protocol was implemented:

-A first wavefront measurement is acquired in a pristine, unprocessed area of the sample, serving as a reference.

-A second wavefront measurement is taken on the laser-processed region of interest.

-The two wavefronts are subtracted to obtain a differential OPD map corresponding exclusively to the modifications induced by the laser.

This differential approach effectively cancels out contributions from the optical system itself (e.g., lens aberrations), isolating the OPD resulting from:

-Surface profile changes (crater depth and shape)

-Subsurface refractive index variations within the heat-affected zone

As a result, the method enables precise, non-destructive mapping of the laser-induced modifications in both geometry and material.

3. Numerical model

To support the experimental analysis and gain deeper insight into the thermal effects of CO_2 laser irradiation on fused silica, a numerical model was developed using COMSOL Multiphysics. This model builds upon previous iterative work [33-35], with the goal of understanding the evolution of surface temperature and the extent of the heat-affected zone (HAZ) as functions of pulse width and power, using experimentally measured crater profiles as key reference data.

Although the core modeling framework has been extensively described in the aforementioned references, we summarize here the key physical assumptions, modeling choices, and computational setup relevant to the present study.

3.1 Model description

We modeled the thermal response of fused silica to CO_2 laser irradiation by solving the time-dependent heat conduction equation within a 2D axisymmetric domain representing a silica block. The laser heat source was applied as a Gaussian distribution at the surface, with a beam waist matching the experimentally measured value. To account for absorption within the bulk, the source intensity was made depth-dependent, incorporating the temperature-dependent complex refractive index of silica as described in [36].

The heat source was active only during the laser pulse duration ($\Delta\tau$), after which it was switched off to simulate the cooling phase. The model supports single or multiple pulses at specified repetition rates. Heat transfer physics included conduction in solids, surface radiation losses, cooling via vaporization, implemented as a boundary condition based on temperature-dependent mass flux. The simulation outputs the temperature distribution within the silica over time, providing insight into both heating and cooling dynamics.

To evaluate structural modifications caused by rapid thermal cycling, we implemented the computation of the fictive temperature, T_f, a parameter that characterizes the glass network's structural state. This was achieved using the Tool–Narayanaswamy model [37], which was solved via an ordinary differential equation (ODE) in COMSOL's mathematics module. A brief description of the equations used to calculate T_f is given in Appendix A.

Material removal by evaporation was estimated using the Hertz–Knudsen equation, incorporating an empirical correction factor to account for atmospheric effects and the complex physical phenomena that reduce the evaporation rate under ambient conditions [35,38].

Additionally, we modeled surface deformation due to densification, which occurs prior to the onset of evaporation. This deformation is linked to structural compaction in regions where the material remains below the evaporation threshold but above the glass transition temperature. The densification was calculated based on the relationship between fictive temperature and material density, as established by [22].

This comprehensive model, more detailed in [35], allows simultaneous evaluation of temperature profiles, evaporation-driven ablation, and surface changes due to densification—offering predictive insight into the interplay between laser parameters and material response.

3.2 Material parameters

The thermo-physical parameters implemented in the model for the simulations reported in this work are summarized in Table 1.

3.3 Solver configuration

In COMSOL Multiphysics, the heat transfer simulation was conducted using the Heat Transfer Module within a 2D axisymmetric configuration. This approach takes advantage of the axial symmetry of both the laser beam and its normal

incidence on the silica surface. The computational domain consists of a 4 × 2 mm² block, discretized using a free triangular mesh. A minimum mesh size of 0.8 μm was applied near the symmetry axis to accurately resolve steep temperature gradients and fine surface features.

For solving the heat equation, we employed the PARDISO direct linear solver, with a relative tolerance set to 0.01. Time integration was performed using the Backward Differentiation Formula (BDF) method with intermediate steps, suitable for capturing the rapid transient thermal responses induced by pulsed laser irradiation.

To model the dynamic surface evolution due to material evaporation, we implemented a velocity-based moving mesh using the Arbitrary Lagrangian–Eulerian (ALE) method. The surface deformation is governed by a prescribed normal mesh velocity, corresponding to the evaporation front velocity, and applied specifically on the irradiated surface region where the heat source is active. This approach enables a simple but realistic simulation of crater formation and surface reshaping.

4. Results and discussion

A series of laser irradiation experiments was performed on the fused silica samples, covering a broad range of single pulse irradiations from a few microseconds to several seconds. The objective was to compare the resulting surface morphologies and heat-affected zones (HAZ) across different thermal regimes. Due to the constraints imposed by the available laser power and beam diameter, a minimum pulse duration of 15 μs was required to observe measurable surface modifications, corresponding to a peak intensity of 5.8×10^5 W/cm² and a pulse fluence of 8.7 J/cm² (74 W reach the sample). The maximum pulse duration was set to a few seconds, enabling exploration of deep thermal diffusion effects.

To facilitate interpretation, the analysis is structured into three temporal regimes based on pulse duration: microsecond regime (μs), millisecond regime (ms), second regime (s). This categorization spans nearly six orders of magnitude in time, allowing a clear comparison of the dominant physical processes governing material response in each case. For each set of pulse duration (μs, ms and s) the laser power was kept constant and the pulse duration gradually increased. The results are presented in two parts: surface morphology analysis, focusing on crater geometry and ablation characteristics; Heat-affected zone analysis, including spatial extent and estimation of material property changes (e.g., refractive index and density) related to thermal effects.

4.1 Surface profile

The selected range of laser parameters—specifically pulse duration and average power—was chosen to generate surface pits with sub-micrometer depths. Operating in this low-evaporation regime allows the formation of smooth and shallow craters, which are ideally suited for high-resolution optical profilometry and fall within the scope of our numerical modeling capabilities [34,35]. This controlled regime avoids conditions where fluid dynamics (e.g., melt flow or resolidification instabilities) dominate, which would fall outside the assumptions of our current model, as it does not incorporate Navier-Stokes-based fluid motion. Additionally, for longer pulse durations or higher energy deposition leading to deeper features, profile measurements become less reliable due to steep crater walls, limited optical access, and increased surface roughness.

Table 1 Thermo-physical properties of fused silica used in the simulations.

Property	Description	Ref.
Refractive index	2.2	35
Extinction coefficient	$1.82\times10^{-2}+10.1\times10^{-5}(T - 273.15)$	23
Emissivity	0.8	23
Thermal conductivity (W/m/K)	$0.92885 + (1.43183\times10^{-3})T$ for 273 K < T < 1390 K $5.56413 - (1.9029\times10^{-3})T$ for 1390 K < T < 1873 K 2 for T > 1873 K	23
Specific Heat (J/kg/K)	$-120+4.56T-(7.38\times10^{-3})T^2+(6.5913\times10^{-6})T^3-(3.0557\times10^{-9})T^4+(5.7158\times10^{-13})T^5$ for 273 K < T < 1500 K $678.25 - 0.1423T+(3.451\times10^{-4})T^2$ for 1500 K < T < 1696 K 1429.5 for T > 1696 K	23
Density (kg/m³)	2201	23
Density change with T_f (kg/m³/K)	9.3×10^{-3}	22
Boiling Temp.	3085	35
Initial T_f (K)	1315	28
Structural relaxation time (s)	1.064×10^{-17}	37
Molecular weight in vapor phase (kg/mol)	40×10^{-3}	23
Vaporization enthalpy (kJ/mol)	425	23
Effective evaporation coefficient	0.82	35

Figure 3 presents representative surface profiles obtained for various sets of laser parameters. The profiles show how crater depth and diameter evolve with increasing pulse duration and fluence.

The measured geometries exhibit Gaussian-like depressions, consistent with the spatial intensity distribution of the focused CO_2 beam. However, despite exhibiting globally similar crater geometries, the different laser regimes reveal notable morphological differences attributed to different physical effect: evaporation, flow, and densification are known to contribute to the pit shape [38]. In the microsecond (μs) regime, craters are typically well-defined and symmetric, with clean, rim-free edges, indicating localized evaporation with minimal thermal diffusion or melt dynamics. In contrast, pulses exceeding 1 second induce the formation of

a raised rim or bump around the crater periphery. This is attributed to significant molten flow and resolidification during and after the laser pulse, suggesting the surface has remained above the softening point for a sufficient duration to enable glass flow [38]. Even in the millisecond (ms) regime, such features begin to appear, albeit more subtly. Another noteworthy feature is the slope discontinuity or break at the edge of the crater, clearly visible in the profiles shown in Figure 3(d) and 3(f) (black plots). This slope break appears prior to any molten flow and is interpreted as a signature of surface densification in the heat-affected zone (HAZ), where the temperature was high enough to restructure the glass network but insufficient to trigger strong evaporation. This densification, driven by rapid thermal cycling and the associated increase in fictive temperature, leads to volume shrinkage and a local depression of the surface [22,23,28,38]. In the µs regime, this effect is not observed, likely due to the limited thermal penetration and minimal HAZ thickness, making the structural changes too shallow to influence surface topography measurably.

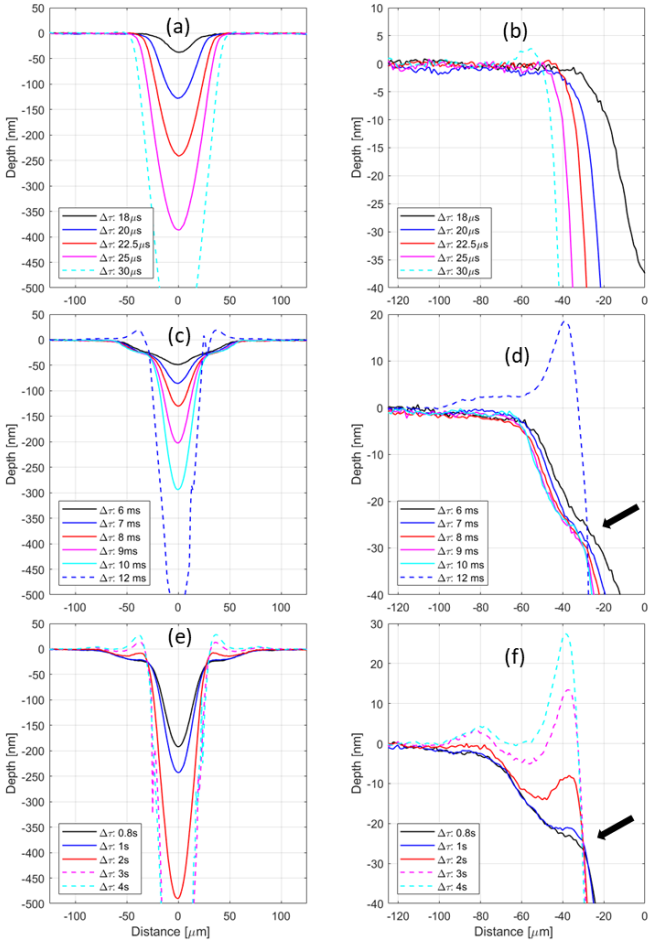

Fig. 3 Measurement of pit profiles with Optical Profilometry for different pulse durations. (a) and (b) corresponds to 76 W of CO_2 laser power (corresponding to an intensity of $3x10^5$ W/cm²), (c) and (d) to 1.75 W ($6.9x10^3$ W/cm²), (e) and (f) to 1.2 W ($4.7x10^3$ W/cm²). The figures on the left displays a cut of the profile passing through the center of the craters. The figures on the right displays a focus on the edges of the craters. Black arrows point to the discontinuities or slope breaks discussed in the

To further investigate these phenomena, we applied the numerical model described in Section 3, using the experimental parameters—pulse duration, laser power, and spot size—as inputs. The simulations are restricted to the cases that does not involves raised rims as their formation involves melt fluid flow that is not taken into account in our model. Figure 4 presents selected comparisons between simulated and measured surface profiles for three representative experimental conditions, each yielding similar pit depths but corresponding to distinct thermal regimes.

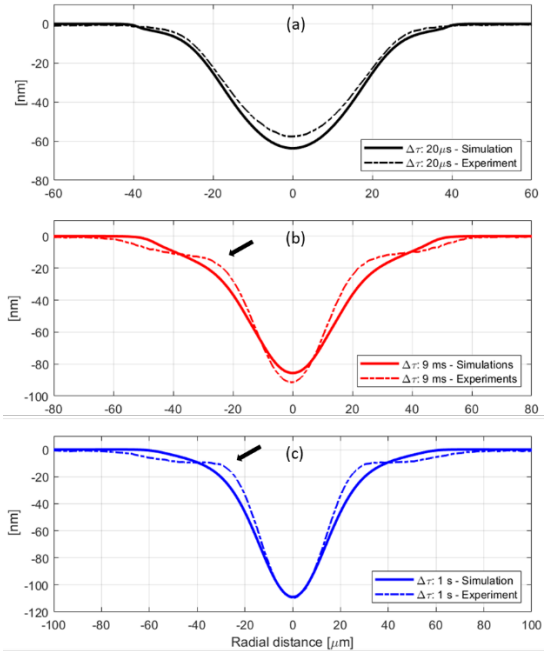

Fig. 4 Comparison of the simulated and measured surface profiles for 3 different experimental parameters: 20 µs, $3x10^5$ W/cm² ; 9 ms, $6.9x10^3$ W/cm² ; 0.8 s, $4.7x10^3$ W/cm². Black arrows point to the discontinuities or slope breaks discussed in the

The calculated pit depths, obtained with silica properties reported in Table 1, show good agreement with the experimental measurements. This confirms the robustness of our understanding of the evaporation mechanism, even when extrapolated from conditions significantly different from those in [35]—notably in terms of spot size and pulse duration. Figure 5 summarizes the comparison between simulated and measured pit depths, demonstrating that the model accurately predicts the ablation depth across a wide range of laser parameters.

However, discrepancies remain at the edges of the pits, particularly for ms and s pulse durations (as illustrated in Fig. 4). These differences point to limitations in the current modeling of the densification process, especially in peripheral regions of the heat-affected zone. This behavior aligns with previous observations reported in [34], where surface deformation due to densification was underestimated by simulations.

Given that density variations in silica are intrinsically linked to refractive index changes [25,26], this motivates a more detailed analysis of the optical phase measurements, which provide direct insight into the magnitude and spatial extent of the heat-affected zone (HAZ). This analysis is presented in the following section.

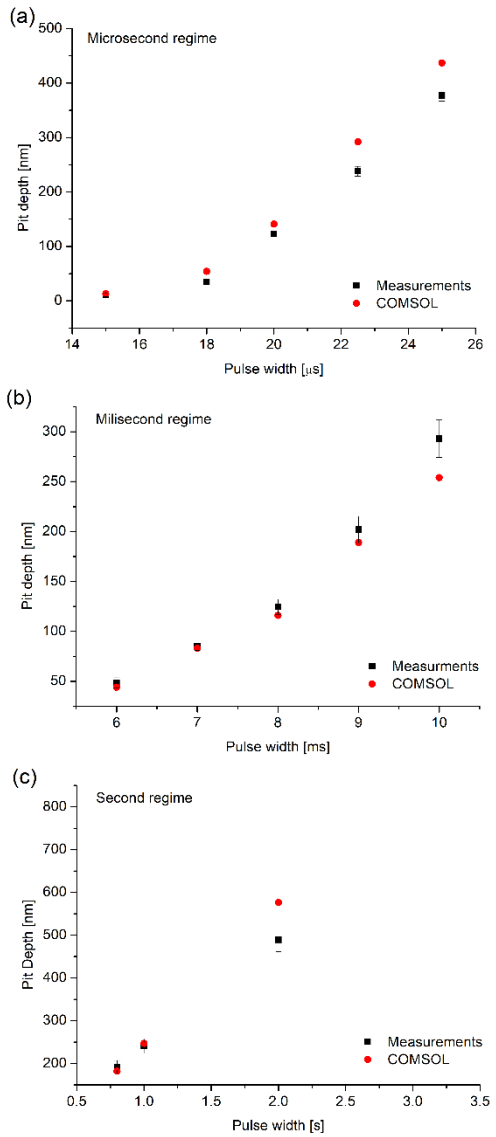

Fig. 5 Measured and calculated depth at the center of the pits, for the different range of pulse durations: (a) 20 µs, 3x10^5 W/cm² ; (b) 9 ms, 6.9x10^3 W/cm² ; (c) 0.8 s, 4.7x10^3 W/cm².

4.2 Heat affected zone

HAZ is characterized in fused silica with a change of fictive temperature, associated to modification of refractive index. The quantitative-phase microscope described in Section 3 provides spatial maps of the optical path difference (OPD)—expressed in nanometers—between pristine silica and the laser-processed region. Two distinct terms contribute to the measured OPD:

-The optical delay caused by the pit itself, which is:

$$OPD_{pit} = (n_{silica} - n_{air})e, \quad (1)$$

where n_{silica}=1.457 at 22 °C (Corning data), n_{air}=1, and e(x,y) is the local crater depth obtained from optical profilometry.

-The optical delay caused by the refractive-index changes (sub-surface modification). Laser heating densifies the glass network in the HAZ, producing a depth-dependent index change Δn(z) that is a priori unknown.

Because OPD_{pit} can be calculated directly from the measured surface profile, it is possible to isolate the HAZ contribution:

$$OPD_{HAZ} = OPD_{total} - OPD_{pit}. \quad (2)$$

Figure 6 illustrates this procedure for a representative millisecond pulse. Surface-profile data were first interpolated onto the QPM grid, and the two datasets were spatially registered with a custom MATLAB routine to compensate for the difference in imaging systems. After subtraction, the residual phase map reveals a positive OPD under the crater, indicating a local increase in refractive index consistent with density rise in the densified zone.

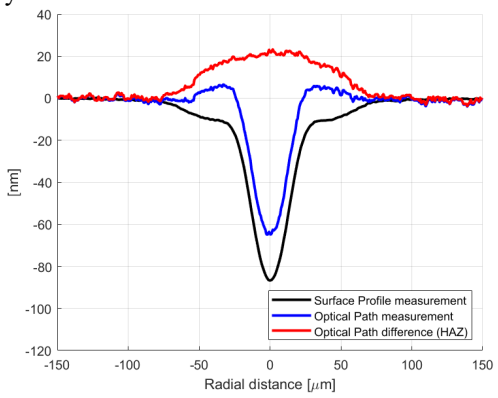

Fig. 6 Illustration of the retrieval of the Optical Path Difference related to the HAZ on a laser-processed pit (0.8 s, 4.7x10^3 W/cm²).

Figure 7 compiles OPD_{HAZ} profiles for all pulse durations studied. In every case the HAZ yields a positive phase shift. The magnitude and lateral extent of this phase signature grow systematically from the µs to the s regime.

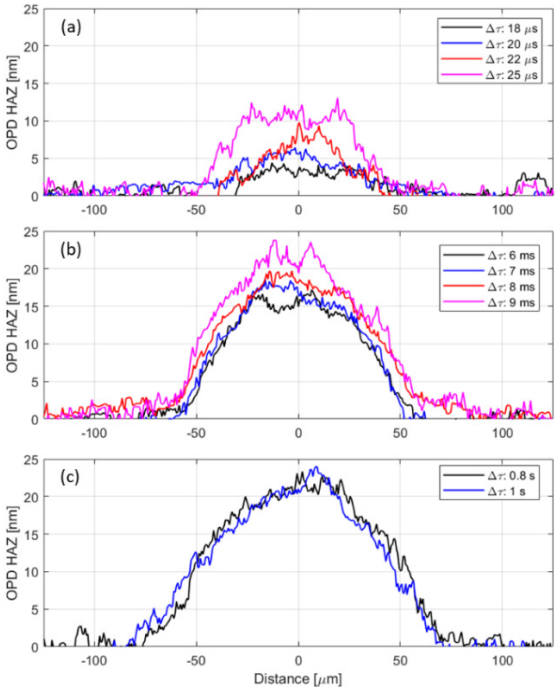

Fig. 7 The retrieved OPD of the HAZ in the different laser-processed sites: (a) 20 µs, 3x10^5 W/cm² ; (b) 9 ms, 6.9x10^3 W/cm² ; (c) 0.8 s, 4.7x10^3 W/cm².

These quantitative OPD maps therefore provide a direct, non-destructive measurement of the heat-affected zone (HAZ) thickness and of the refractive index changes induced by laser processing— two key metrics to study the densification based on the multiphysics model introduced in Section 3. As illustrated in Figure 6, the OPD contribution attributed to the HAZ is positive. This is consistent with an increase in material density within the laser-affected volume, leading to a corresponding increase in refractive index, as previously reported in densified silica systems [25,26].

Further analysis of OPD maps across the range of tested pulse durations reveals a clear evolution of the HAZ with increasing pulse width. From microsecond to second-scale pulses, the OPD amplitude increases markedly, indicating a deepening and broadening of the densified zone. This trend reflects the extended thermal diffusion enabled by longer interaction times. Additionally, the shape of the OPD profiles exhibits a notable transition. For short pulses in the microsecond regime, the OPD distribution shows a nearly flat-top profile, centered around the crater area. This indicates a confined and relatively uniform densification zone resulting from rapid heating and cooling, with negligible lateral thermal spread. In contrast, for millisecond and second-scale pulses, the OPD profiles take on a bell-shaped form, broader than the crater and smoothly decreasing toward the periphery. This behavior is indicative of a graded refractive index change caused by gradual thermal diffusion away from the irradiated zone during longer pulses.

To gain further insight into these trends, numerical simulations of the fictive temperature evolution were performed using the model described in Section 3. The simulations provide the spatial distribution of fictive temperature changes in the material, which are directly linked to structural relaxation and density variations. Figure 8 shows the simulated contours of fictive temperatures for three representative pulse durations: 20 µs, 9 ms, and 0.8 s. The conditions have been selected so that they give the same crater depth (see Fig. 4) but with significant differences for the heat affected zone.

Comparison of the three representative pulse regimes confirms that the heat-affected zone shrinks dramatically when the laser pulse duration is reduced. For microsecond irradiation the fictive-temperature field extends no more than ~5 µm beneath the surface and remains remarkably uniform, whereas second-long pulses drive structural changes to depths approaching 30 µm and generate a pronounced thermal gradient; millisecond pulses occupy an intermediate position between these two extremes.

Because fictive temperature is directly linked to network compaction, the corresponding density increase can be estimated from Shelby's calibrated coefficient, $\Delta\rho = 9.3$ g/m^3/K [22]. Compaction in turn raises the local refractive index. Although published values of dn/dT_f vary with OH content, the coefficients reported by Kakiuchida et al. [25] and Haken et al. [26] cluster around 1.0×10^{-6} K^{-1}. We adopted a representative value of 1.1×10^{-6} K^{-1} and coupled it to the simulated T_f field to obtain a theoretical OPD map for each pulse condition.

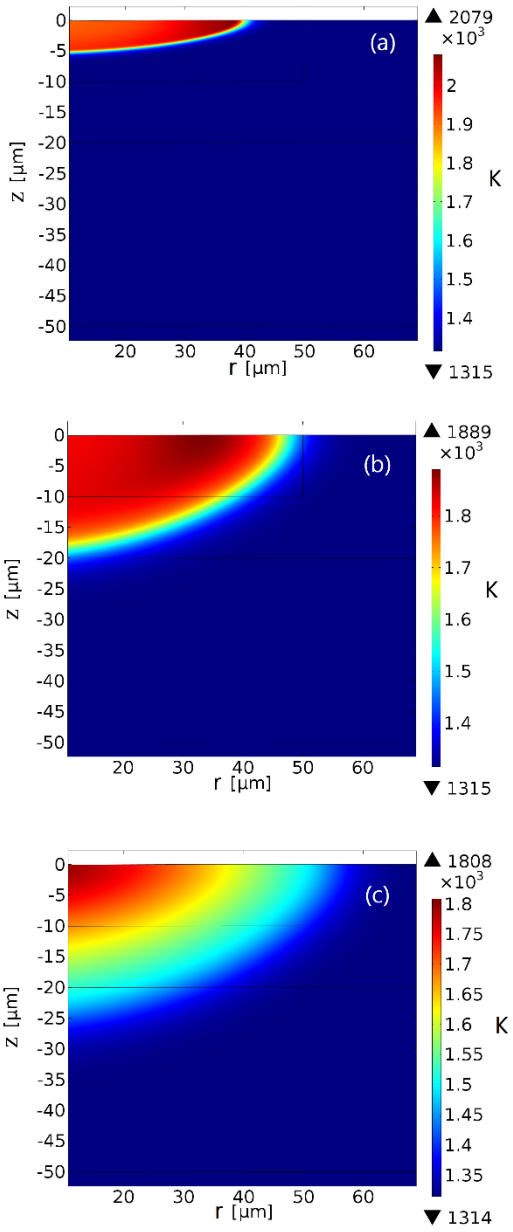

Fig. 8 Comparison of the spatial distribution of fictive temperatures for pulse widths of (a) 20 µs, 3x10^5 W/cm² ; (b) 9 ms, 6.9x10^3 W/cm² ; (c) 0.8 s, 4.7x10^3 W/cm². T_f is obtained at a time much larger than the irradiation time scale.

Figure 9 juxtaposes these calculated OPD profiles with the experimental phase data for the three benchmarks.

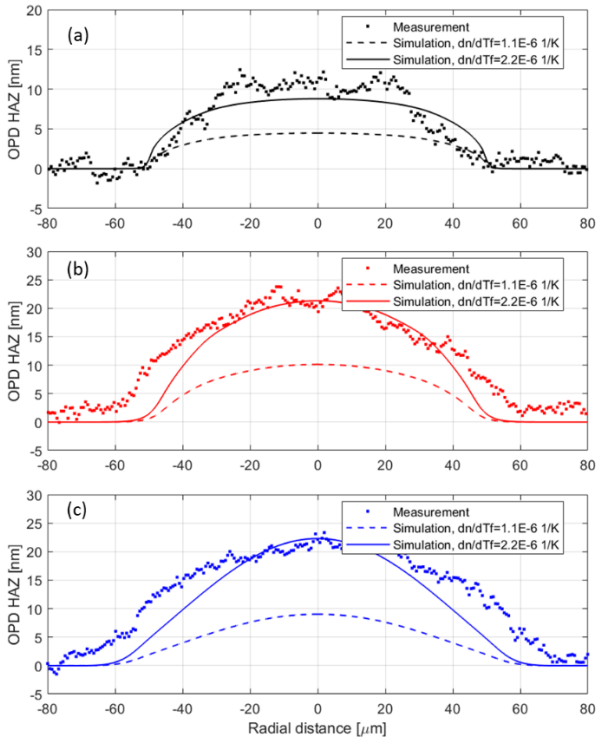

Fig. 9 Comparison of the measured OPD of the HAZ and its comparison to simulations with different dn/dTf, for the following conditions: (a) 25 µs, 3x10^5 W/cm² ; (b) 9 ms 6.9x10^3 W/cm² ; (c) 1s, 4.7x10^3 W/cm².

A notable discrepancy emerges when comparing the theoretical OPD values derived from the model to those obtained experimentally. As illustrated in Figure 9, the simulated phase shifts underestimate the measurements by nearly a factor of two. To achieve agreement, the refractive index dependence on fictive temperature must be adjusted to dn/dT_f=2.2x10^{-6} K^{-1}, which is twice the typical values reported in the literature. Although this adjustment currently lacks independent validation, several plausible explanations can be proposed. First, some studies do report higher refractive index sensitivities than the values adopted in earlier sections. For example, data extracted from Tan et al. [39] yield a coefficient of dn/dT_f=2.0×10^{-6} K^{-1}, which is consistent with our findings and supports the hypothesis that higher values may indeed apply under certain conditions. We can also mention the values reported by Ponader et al [40] in the range of 1.7x10^{-6} K^{-1}. Second, the laser irradiation process induces extreme thermal environments, with localized temperatures approaching or exceeding the boiling point of silica (~3000 K). Such high temperatures are likely to alter the local chemical composition of the fused silica, notably by reducing the concentration of hydroxyl (OH) or molecular water (H_2O) species. According to Kuzuu et al. [41], these compositional shifts can impact the refractive index independently of structural densification, introducing an additional layer of complexity not captured in models calibrated using moderate-temperature annealing data. These observations suggest the need for a deeper analysis of the heat affected zone, by coupling for instance the methodology we have developed in the present work to spatially resolved structural diagnostics such as confocal Raman spectroscopy, to directly probe the network structure and composition of the heat-affected zone.

5. Conclusion

In this work, we have investigated the influence of laser pulse duration on surface and subsurface modifications in fused silica, covering a wide temporal range from microseconds to seconds. By combining experimental techniques—including optical profilometry and quantitative phase microscopy—with a multiphysics numerical model incorporating thermal diffusion, material evaporation, densification, and fictive temperature evolution, we provided a comprehensive picture of both crater formation and heat-affected zones (HAZ).

The surface profile measurements revealed a smooth and regular morphology in the µs regime, while longer pulses (ms to s) led to more pronounced effects such as rim formation and slope discontinuities—features attributed respectively to molten material flow and densification-driven volume shrinkage. Numerical simulations successfully predicted pit depths across different regimes, validating the accuracy of the effect of thermal-evaporation in the model, though discrepancies at the crater edges indicates limitations in the current densification implementation.

Subsurface characterization using OPD maps enabled the direct, non-invasive quantification of HAZ extension and refractive index modification. The experimental OPD showed a clear increase with pulse duration, associated with deeper and more gradient-like thermal penetration. By correlating fictive temperature profiles to density and refractive index changes, we simulated the phase shift induced by the HAZ and compared it to measurements. Although the model captured the qualitative behavior, quantitative agreement required assuming a higher dn/dT_f value than commonly reported. This discrepancy points to potential laser-induced compositional changes, such as OH content reduction, which are not accounted for in our model.

This study advances the predictive capabilities for laser processing of transparent materials and supports the optimization of microstructuring techniques in optics and photonics applications.

Appendix A
Fictive temperature

The fictive temperature T_f is a concept in glass science that characterizes the structural state of a glass. It defines the temperature at which the viscoelastic liquid state is in structural equilibrium with the metastable solid state during the silica glass cooling phase [37]. In our numerical simulations, we used the Tool-Narayanaswamy model to calculate T_f:

$$\frac{dT_f}{dt} = \frac{T - T_f}{\tau(T, T_f)}, \tag{3}$$

where T is the material temperature, and $\tau(T, T_f)$ is the glass structural relaxation time which depends on both the physical temperature T as well as the fictive temperature T_f. The structural relaxation time τ is given by:

$$\tau = \tau_\infty \exp\left\{\frac{\Delta H_r}{R_c}\left[\frac{x}{T} + \frac{1-x}{T_f}\right]\right\}, \tag{4}$$

where τ_∞ is a relaxation time measured at $T = \infty$, R_c is the universal gas constant, ΔH_r is the activation enthalpy for structural relaxation with a value of 457 kJ/mol [33], and x is the contribution of the activation energies from the thermodynamic and fictive temperature. We use a value of $x = 0.9$ based on previous experimental measurements [42].

References

[1] F. Nürnberg, B. Kühn, A. Langner, M. Altwein, G. Schötz, R. Takke, S. Thomas, and J. Vydra: Proc. SPIE, Vol. 9632, (2015) 96321R.
[2] C.W. Carr, Proc. SPIE, Vol. 12726, (2023) 1272602.
[3] T. I. Suratwala, P. E. Miller, J. D. Bude, W. A. Steele, N. Shen, M. V. Monticelli, M. D. Feit, T. A. Laurence, M. A. Norton, C. W. Carr, and L. L. Wong: J. Am. Ceram. Soc., 94, (2011) 416.
[4] L. Sun, J. Huang, H. Liu, X. Ye, J. Wu, X. Jiang, L. Yang, W. Zheng, and W. Wu: Opt. Lett., 41, (2016) 4464.
[5] N. Bonod, P. Brianceau, and J. Néauport: Optica, 8, (2021), 1372.
[6] J. Neauport, L. Lamaignere, H. Bercegol, F. Pilon, and J.-C. Birolleau: Opt. Express, 13, (2005) 10163.
[7] R. A. Negres, G. M. Abdulla, D. A. Cross, Z. M. Liao, and C. W. Carr: Opt. Express, 20, (2012) 13030.
[8] L. Lamaignère, G. Dupuy, A. Bourgeade, A. Benoist, A. Roques, and R. Courchinoux: Appl. Phys. B, 114, (2014) 517.
[9] R. M. Brusasco, B. M. Penetrante, J. A. Butler, and L. W. Hrubes: Proc. SPIE, Vol. 4679, (2002) 40.
[10] E. Mendez, K. M. Nowak, H. J. Baker, F. J. Villarreal, and D. R. Hall: Appl. Opt., 45, (2006) 5358.
[11] A. During, P. Bouchut, J. G. Coutar, C. Leymarie, and H. Bercegol: Proc. SPIE, 6403, (2007) 40323.
[12] I. L. Bass, G. M. Guss, M. J. Nostrand, and P. J. Wegner: Proc. SPIE, Vol. 7842, (2010) 784220.
[13] W. Dai, X. Xiang, Y. Jiang, H. J.Wang, X. B. Li, X. D. Yuan, W. G. Zheng, H. B. Lv, and X. T. Zu: Opt. Lasers Eng., 49, (2011) 273.
[14] P. Cormont, A. Bourgeade, S. Cavaro, T. Donval, T. Doualle, G. Gaborit, L. Gallais, L. Lamaignère, and J.-L. Rullier: Adv. Eng. Mater., 17, (2005) 253.
[15] C. Weingarten, A. Schmickler, E. Willenborg, K. Wissenbach, and R. Poprawe: J. Laser Appl., 29, (2017) 011702.
[16] L. Zhao, J. Cheng, M. Chen, X. Yuan, W. Liao, Q. Liu, H. Yang, and H.Wang: Int. J. Extrem. Manuf., 1, (2019) 035001
[17] M. Kahle, D. Conrad, S. Fricke, and L. Wilkens: J. Laser Micro Nanoeng., 17, (2022) 156.
[18] K.Okazaki, S.Torii, T.Makimura, H.Niino, K.Murakami, D.Nakamura, A.Takahashi, and T.Okada: J. Laser Micro Nanoeng., 5, (2010) 269.
[19] B. K. Nayak, R. Akaparu, J. P. Carberry, and A Liu: J. Laser Micro Nanoeng., 9, (2014) 79.
[20] H.-K. Choi, J. Ryu, C. Kim, Y.-C. Noh, I.-B. Sohn, and J.-T. Kim: J. Laser Micro Nanoeng., 11, (2016) 341.
[21] V. Zandian, J. S. Florry, and D. Taylor: Br. Ceram. Trans. J., 90, (1991) 59.
[22] J. E. Shelby: J. Non-Cryst. Solids, 349, (2004) 331.
[23] T. Doualle, L. Gallais, P. Cormont, D. Hébert, P. Combis, and J. L. Rullier: J. Appl. Phys., 119, (2016) 113106.
[24] T. Doualle, L. Gallais, S. Monneret, S. Bouillet, A. Bourgeade, C. Ameil, L. Lamaignère, and P. Cormont: Opt. Eng., 56, (2017) 011022.
[25] H. Kakiuchida, E. H. Sekiya, N. Shimodaira, K. Saito, and A. J. Ikushima: J. Non-Cryst. Solids, 353, (2007) 568.
[26] U. Haken, O. Humbach, S. Ortner, and H. Fabian: J. Non-Cryst. Solids, 265, (2000) 9.
[27] M. J. Matthews, R. M. Vignes, D. Cooke, S. T. Yang, and J. S. Stolken: Opt. Lett., 35, (2010) 1311.
[28] A. E. M. Browar, N. J. Ray, M. J. Matthews, N. Shen, G. Guss, N. Carlie, and J. D. Ellis: J. Appl. Phys., 130, (2021) 115302.
[29] J. Sullivan, J. Zhao, and T. D. Bennett: Appl. Opt., 44, (2005) 7173.
[30] J. Zhao, J. Sullivan, J. Zayac, and T.D. Benett: J. Appl. Phys., 95, (2024) 5475.
[31] T. Doualle, A. Ollé, P. Cormont, S. Monneret, and L. Gallais: Opt. Lett., 42, (2017) 1616.
[32] P. Bon, G. Maucort, B. Wattellier, and S. Monneret: Opt. Express, 17, (2009) 13080.
[33] T. Doualle, L. Gallais, P. Cormont, D. Hebert, P. Combis, and J.-L. Rullier: J. Appl. Phys., 119, (2016) 113106.
[34] C. Cifuentes-Quintal, P. Cormont, and L. Gallais: J. Appl. Phys., 130, (2021) 093106.
[35] L. A. Vazquez-Zuniga, C. Galvan, J.-F. Gleyze, P. Cormont, and L. Gallais: J. Appl. Phys., 137 (2025) 135106.
[36] A. D. McLachlan and F. P. Meyer: Appl. Opt., 26, (1987) 1728.
[37] R. Vignes, T. Soules, J. Stolken, R. Settgast, S. Elhadj, and M. Matthews: J. Am. Ceram. Soc., 96, (2013) 137.
[38] S. Elhadj, M.J. Matthews, G.M. Guss, and I.L. Bass: Appl. Phys. B, 113, (2013) 307.
[39] C.Z. Tan, and J. Arndt: Physica B: Condensed Matter, 229, (1997) 217.
[40] C. W. Ponader, J. F. Schroeder, and A. M. Streltsov: J. Appl. Phys., 103, (2008) 063516.
[41] N. Kuzuu, J.W. Foley, and N. Kamisugi: J. Ceram. Soc. Jap., 105, (1998) 525.
[42] L. Robin, P. Combis, P. Cormont, L. Gallais, D. Hebert, and C. Mainfray: J. Appl. Phys., 111, (2012) 63106.

(Received: June 26, 2025, Accepted: December 5, 2025)